Multiscale Modeling of Incompressible Turbulent Flows

T. Y. Hou[a], X. Hu[a,*], F. Hussain[b]

[a] *Applied and Computational Mathematics, California Institute of Technology, Pasadena, CA 91125, USA*
[b] *Department of Mechanical Engineering, University of Houston, Houston, TX 77204, USA*

Abstract

Developing an effective turbulence model is important for engineering applications as well as for fundamental understanding of the flow physics. We present a mathematical derivation of a closure relating the Reynolds stress to the mean strain rate for incompressible flows. A systematic multiscale analysis expresses the Reynolds stress in terms of the solutions of local periodic cell problems. We reveal an asymptotic structure of the Reynolds stress by invoking the frame invariant property of the cell problems and an iterative dynamic homogenization of large- and small-scale solutions. The recovery of the Smagorinsky model for homogeneous turbulence validates our derivation. Another example is the channel flow, where we derive a simplified turbulence model using the asymptotic structure near the wall. Numerical simulations at two Reynolds numbers (Re's) using our model agrees well with both experiments and Direct Numerical Simulations of turbulent channel flow.

Keywords:
Turbulence modeling, Multiscale analysis, Smagorinsky model, Channel flow

1. Introduction

Turbulence has been a central research area in fluid dynamics since the 19th century. The Navier-Stokes equation, one of the seven millennium prize

*Corresponding author
Email addresses: hou@cms.caltech.edu (T. Y. Hou), lanxin@cms.caltech.edu (X. Hu), fhussain@uh.edu (F. Hussain)
URL: http://users.cms.caltech.edu/~hou (T. Y. Hou)

problems established by the Clay Mathematics Institute, gives a good description of turbulent flows, according to extensive theoretical and experimental works. However, it is still an open question whether the solution of the 3D incompressible Navier-Stokes equation with smooth initial data and with finite energy will remain smooth for all times. In addition, it is extremely difficult to solve the Navier-Stokes equation due to its non-local nonlinear nature.

The enormous progress of computer technology has enabled direct numerical simulation (DNS) of the Navier-Stokes equation. But tremendous computing resource is still required to perform DNS of turbulent flows, especially at a high Re and/or irregular geometry. Many turbulence models have been developed, aiming at capturing the most important statistical quantities of turbulent flows, such as profiles of mean velocity, r.m.s. velocity fluctuations, etc. . Among them, the eddy-viscosity models were the first. But they over-simplify the turbulent structures without considering the essential physical mechanisms. Another popular model is the Smagorinsky model [1] and its variants[2, for an example of channel flow], which have succeeded in many applications, e.g. homogeneous turbulence and channel flow.

Large eddy simulation (LES) has calculated practical flows even in relatively complex geometries [3, 4, 5, 6]. However, it is still impossible to simulate the wall-bounded flows at high Re, since a huge number of grid points are needed to resolve the small structure near the wall [7, 8]. Recently, hybrid models, which combine LES with Reynolds Averaged Navier Stokes (RANS) equation, have been proposed to improve the modeling performance [9, 10]. Most popular RANS models yield good predictions of high Re turbulent flows. Hence, the RANS model is applied near the wall, and LES away from the wall. Spalart et al. [8] proposed the detached eddy simulation (DES) by modifying the Spalart-Allmaras one-equation model. The RANS simulation in the near-wall region is switched to the LES in the outer region, where the model length scale is changed from the wall distance to a pseudo-Kolmogorov length scale. DES has been applied to predict separated flow around a rounded square corner [11]. All these models, however, are based on speculative formulations and/or fittings to experimental data. No systematic mathematical derivation of such a model has been possible yet.

In this paper, we present a mathematical derivation based on a multiscale analysis of Navier-Stokes equations developed by Hou-Yang-Ran [12, 13, hereafter referred to as HYR], aiming to systematically derive the Reynolds stress for 3D homogeneous incompressible Euler and Navier-Stokes equations.

A multiscale model can be obtained by separating variables into large- and small-scale components and considering the interactions between them. This gives rise to a system of coupled equations for large- and small-scales. An important feature of the multiscale formulation is that no closure assumption is required and no unknown parameters to be determined. Therefore, it provides a self-consistent multiscale system, which captures the dynamic interaction between the mean and small-scale velocities. This multiscale technique has been successfully applied to 3D incompressible Navier-Stokes equation with multiscale initial data [13]. It couples the large-scale solution to a subgrid cell problem. The computational cost is still quite high but an adaptive scheme has speeded up the computation.

In the multiscale model, the Reynolds stress term is expressed as the average of tensor product of the small-scale velocities, which are the solutions of a local periodic cell problem. By using the frame invariance property of the cell problem and an iterative homogenization of large- and small-scale solutions dynamically, we reveal a crucial structure of the Reynolds stress and obtain an explicit form of it. This seems to be the first linear constitutive relation between the Reynolds stress and the strain rate, established by combining a systematic mathematical derivation with physical arguments.

For homogeneous turbulence, we recover the Smagorinsky model using least assumptions, while a simplified Smagorinsky model can be derived given the structure of turbulent channel flow. A numerical study validates the simplified model for channel flow, with good agreement of the mean velocity with both experimental and DNS results at $Re_\tau = 180$ and $Re_\tau = 395$. An extensive numerical study is reported in [14], which shows good qualitative agreement of the simplified model with DNS and experimental data.

The paper is organized as follows: In section 2, we briefly review the multiscale analysis for the 3D Navier-Stokes equation. The systematic mathematical derivation, based on the multiscale analysis is presented in section 3. In section 4, the Smagorinsky model for homogeneous turbulence is recovered via this mathematical derivation. A simplified Smagorinsky model is obtained for turbulent channel flow and the coefficients in the model are determined and justified. Numerical simulations are carried out to validate the simplified model. Final conclusions and remarks appear in section 5.

2. Multiscale analysis for the 3D Navier-Stokes equation

Based on the multiscale analysis in [12, 13], we can formulate a multiscale system for the incompressible 3D Navier-Stokes equation as a homogenization problem with ϵ being a reference wave length as follows:

$$\partial_t \boldsymbol{u}^\epsilon + (\boldsymbol{u}^\epsilon \cdot \nabla)\boldsymbol{u}^\epsilon + \nabla p^\epsilon = \nu \Delta \boldsymbol{u}^\epsilon, \tag{1}$$

$$\nabla \cdot \boldsymbol{u}^\epsilon = 0, \tag{2}$$

$$\boldsymbol{u}^\epsilon|_{t=0} = \boldsymbol{U}(\boldsymbol{x}) + \boldsymbol{W}(\boldsymbol{x}, \boldsymbol{z}), \tag{3}$$

where $\boldsymbol{u}^\epsilon(\boldsymbol{x}, t)$ and $p^\epsilon(\boldsymbol{x}, t)$ are the velocity field and the pressure, respectively. The initial velocity field $\boldsymbol{u}^\epsilon(\boldsymbol{x}, 0)$ can be reparameterized in a two-scale structure: the mean $\boldsymbol{U}(\boldsymbol{x})$ and the fluctuating $\boldsymbol{W}(\boldsymbol{x}, \boldsymbol{z})$ components. In general, $\boldsymbol{W}(\boldsymbol{x}, \boldsymbol{z})$ is periodic in $\boldsymbol{z}$ with zero mean, i.e.,

$$\langle \boldsymbol{W} \rangle \equiv \int \boldsymbol{W}(\boldsymbol{x}, \boldsymbol{z})\, d\boldsymbol{z} = \boldsymbol{0}.$$

In Appendix A, the reparameterization of the initial velocity $\boldsymbol{u}^\epsilon(\boldsymbol{x}, 0)$ in two-scale structure for channel flow is illustrated. Here, the mean $\boldsymbol{U}(\boldsymbol{x})$ and the fluctuation $\boldsymbol{W}(\boldsymbol{x}, \boldsymbol{z})$ depend on the reference scale ϵ. In the limit $\epsilon \to 0$, $\boldsymbol{W}(\boldsymbol{x}, \boldsymbol{z})$ tends to zero, and the mean $\boldsymbol{U}(\boldsymbol{x})$ recovers the full velocity field, containing all of the scales.

In the analysis, the key idea is a nested multiscale expansion to characterize the transport of the small scales or the high-frequency component $\boldsymbol{W}(\boldsymbol{x}, \boldsymbol{z})$. The first attempt to use homogenization theory to study the 3D Euler equations with highly oscillating data was carried out by McLaughlin et al. [15]. To construct a multiscale expansion for the Euler equations, they made an important assumption that the oscillation is advected by the mean flow. However, Hou *et al.* performed a detailed study by using the vorticity-stream function formulation [12, 13], and found that the small-scale information is in fact advected by the full velocity $\boldsymbol{u}^\epsilon$, which is consistent with Taylor's hypothesis [16]. To be specific, define a multiscale phase function $\boldsymbol{\theta}^\epsilon(t, \boldsymbol{x})$ as follows:

$$\frac{\partial \boldsymbol{\theta}^\epsilon}{\partial t} + (\boldsymbol{u}^\epsilon \cdot \nabla)\boldsymbol{\theta}^\epsilon = \boldsymbol{0}, \tag{4}$$

$$\boldsymbol{\theta}^\epsilon|_{t=0} = \boldsymbol{x}, \tag{5}$$

which, also called the inverse flow map, characterizes the evolution of the small-scale velocity field.

First, we define the two operators for vector functions. For a vector function $\boldsymbol{f}(x_1, x_2, x_3) = (f_1, f_2, f_3)$, the gradient of $\boldsymbol{f}$ is defined as

$$(\nabla_{\boldsymbol{x}} \boldsymbol{f})_{ij} = \frac{\partial f_j}{\partial x_i},$$

while the differential of $\boldsymbol{f}$ is defined as

$$(D_{\boldsymbol{x}} \boldsymbol{f})_{ij} = \frac{\partial f_i}{\partial x_j}.$$

Based on a multiscale analysis in the Lagrangian coordinates, the following nested multiscale expansions for $\boldsymbol{\theta}^\epsilon$ and the stream function $\boldsymbol{\psi}^\epsilon$ are adopted:

$$\boldsymbol{\theta}^\epsilon = \bar{\boldsymbol{\theta}}(t, \boldsymbol{x}, \tau) + \epsilon \tilde{\boldsymbol{\theta}}(t, \bar{\boldsymbol{\theta}}, \tau, \boldsymbol{z}), \tag{6}$$

$$\boldsymbol{\psi}^\epsilon = \bar{\boldsymbol{\psi}}(t, \boldsymbol{x}, \tau) + \epsilon \tilde{\boldsymbol{\psi}}(t, \bar{\boldsymbol{\theta}}, \tau, \boldsymbol{z}), \tag{7}$$

where $\tau = t/\epsilon, \boldsymbol{z} = \bar{\boldsymbol{\theta}}/\epsilon$. $\bar{\boldsymbol{\theta}}$ and $\bar{\boldsymbol{\psi}}$ are averages of $\bar{\boldsymbol{\theta}}^\epsilon$ and $\boldsymbol{\psi}^\epsilon$ respectively; $\tilde{\boldsymbol{\theta}}$ and $\tilde{\boldsymbol{\psi}}$ are periodic functions in $\boldsymbol{z}$ with zero mean. Now direct computations give the expansion for velocity $\boldsymbol{u}^\epsilon$

$$\boldsymbol{u}^\epsilon = \nabla_{\boldsymbol{x}} \times \bar{\boldsymbol{\psi}} + (D_{\boldsymbol{x}} \bar{\boldsymbol{\theta}}^T \nabla_{\boldsymbol{z}}) \times \tilde{\boldsymbol{\psi}} + \epsilon \nabla_{\boldsymbol{x}} \times \tilde{\boldsymbol{\psi}}, \tag{8}$$

which implies the multiscale expansion

$$\boldsymbol{u}^\epsilon = \bar{\boldsymbol{u}}(t, \boldsymbol{x}, \tau) + \tilde{\boldsymbol{u}}(t, \bar{\boldsymbol{\theta}}, \tau, \boldsymbol{z}), \tag{9}$$

where

$$\begin{aligned} \bar{\boldsymbol{u}}(t, \boldsymbol{x}, \tau) &= \nabla_{\boldsymbol{x}} \times \bar{\boldsymbol{\psi}}, \\ \tilde{\boldsymbol{u}}(t, \bar{\boldsymbol{\theta}}, \tau, \boldsymbol{z}) &= (D_{\boldsymbol{x}} \bar{\boldsymbol{\theta}}^T \nabla_{\boldsymbol{z}}) \times \tilde{\boldsymbol{\psi}} + \epsilon \nabla_{\boldsymbol{x}} \times \tilde{\boldsymbol{\psi}}. \end{aligned}$$

The pressure p^ϵ is similarly expanded:

$$p^\epsilon = \bar{p}(t, \boldsymbol{x}, \tau) + \tilde{p}(t, \bar{\boldsymbol{\theta}}, \tau, \boldsymbol{z}). \tag{10}$$

Substituting (9)-(10) into the Navier-Stokes system (1) and averaging with respect to $\boldsymbol{z}$, the equations for the mean velocity field $\bar{\boldsymbol{u}}(t, \boldsymbol{x}, \tau)$ are obtained with initial and proper boundary conditions:

$$\bar{\partial}_t \bar{\boldsymbol{u}} + (\bar{\boldsymbol{u}} \cdot \nabla_{\boldsymbol{x}})\bar{\boldsymbol{u}} + \nabla_{\boldsymbol{x}} \bar{p} + \nabla_{\boldsymbol{x}} \cdot \langle \tilde{\boldsymbol{u}} \otimes \tilde{\boldsymbol{u}} \rangle = \nu \nabla^2_{\boldsymbol{x}} \bar{\boldsymbol{u}}, \tag{11}$$

$$\nabla_{\boldsymbol{x}} \cdot \bar{\boldsymbol{u}} = 0, \tag{12}$$

$$\bar{\boldsymbol{u}}|_{t=0} = \boldsymbol{U}(\boldsymbol{x}), \tag{13}$$

where $\bar{\partial}_t = \partial_t + \epsilon^{-1}\partial_\tau$. The additional term $\langle \tilde{\boldsymbol{u}} \otimes \tilde{\boldsymbol{u}} \rangle$ in (11) is the well-known Reynolds stress. How to model it is important in both fundamental understanding and engineering applications. In many LES, the Reynolds stress is modeled by some closure assumptions. In contrast, by using the frame invariance property of the cell problem and an iterative homogenization of the large- and small-scale solutions dynamically, we reveal a crucial structure of the Reynolds stress. Then the linear constitutive relation between the Reynolds stress and the strain rate can be established mathematically; see section 3.

Next, substituting (6) into (4) and averaging over $\boldsymbol{z}$ give the equations for $\bar{\boldsymbol{\theta}}(t, \boldsymbol{x}, \tau)$ with initial and proper boundary conditions:

$$\bar{\partial}_t \bar{\boldsymbol{\theta}} + (\bar{\boldsymbol{u}} \cdot \nabla_{\boldsymbol{x}})\bar{\boldsymbol{\theta}} + \epsilon \nabla_{\boldsymbol{x}} \cdot \langle \tilde{\boldsymbol{\theta}} \otimes \tilde{\boldsymbol{u}} \rangle = \boldsymbol{0}, \tag{14}$$

$$\bar{\boldsymbol{\theta}}|_{t=0} = \boldsymbol{x}. \tag{15}$$

To simplify the model further, we consider only the leading order terms of large-scale variables $(\bar{\boldsymbol{u}}, \bar{p}, \bar{\boldsymbol{\theta}})$

$$\bar{\boldsymbol{u}}(t, \boldsymbol{x}, \tau) = \boldsymbol{u}(t, \boldsymbol{x}) + \epsilon \boldsymbol{u}_1(t, \boldsymbol{x}, \tau), \tag{16}$$

$$\bar{p}(t, \boldsymbol{x}, \tau) = p(t, \boldsymbol{x}) + \epsilon p_1(t, \boldsymbol{x}, \tau), \tag{17}$$

$$\bar{\boldsymbol{\theta}}(t, \boldsymbol{x}, \tau) = \boldsymbol{\theta}(t, \boldsymbol{x}) + \epsilon \boldsymbol{\theta}_1(t, \boldsymbol{x}, \tau), \tag{18}$$

and small scale variables $(\tilde{\boldsymbol{u}}, \tilde{p}, \tilde{\boldsymbol{\theta}})$

$$\tilde{\boldsymbol{u}} = \boldsymbol{w}(t, \bar{\boldsymbol{\theta}}, \tau, \boldsymbol{z}) + O(\epsilon), \tag{19}$$

$$\tilde{p} = q(t, \bar{\boldsymbol{\theta}}, \tau, \boldsymbol{z}) + O(\epsilon), \tag{20}$$

$$\tilde{\boldsymbol{\theta}} = \boldsymbol{\Theta}(t, \bar{\boldsymbol{\theta}}, \tau, \boldsymbol{z}) + O(\epsilon). \tag{21}$$

This gives simplified averaged equations, up to first order of ϵ,

$$\partial_t \boldsymbol{u} + (\boldsymbol{u} \cdot \nabla_{\boldsymbol{x}})\boldsymbol{u} + \nabla_{\boldsymbol{x}} p + \nabla_{\boldsymbol{x}} \cdot \langle \boldsymbol{w} \otimes \boldsymbol{w} \rangle = \nu \nabla^2_{\boldsymbol{x}} \boldsymbol{u}, \tag{22}$$

$$\nabla_{\boldsymbol{x}} \cdot \boldsymbol{u} = 0, \tag{23}$$

$$\boldsymbol{u}|_{t=0} = \boldsymbol{U}(\boldsymbol{x}), \tag{24}$$

and

$$\partial_t \boldsymbol{\theta} + (\boldsymbol{u} \cdot \nabla_{\boldsymbol{x}})\boldsymbol{\theta} = \boldsymbol{0}, \tag{25}$$

$$\boldsymbol{\theta}|_{t=0} = \boldsymbol{x}. \tag{26}$$

Then we subtract the averaged equations from the Navier-Stokes equation (1) and the equations for the inverse flow map $\boldsymbol{\theta}^\epsilon$ (4). After some algebraic operations, we obtain the equations for the small-scale variables, to the leading order approximation:

$$\partial_\tau \boldsymbol{w} + D_{\boldsymbol{z}}\boldsymbol{w}\mathcal{A}\boldsymbol{w} + \mathcal{A}^\mathsf{T}\nabla_{\boldsymbol{z}} q - \frac{\nu}{\epsilon}\nabla_{\boldsymbol{z}} \cdot (\mathcal{A}\mathcal{A}^\mathsf{T}\nabla_{\boldsymbol{z}}\boldsymbol{w}) = \boldsymbol{0}, \tag{27}$$

$$(\mathcal{A}^\mathsf{T}\nabla_{\boldsymbol{z}}) \cdot \boldsymbol{w} = \boldsymbol{0}, \tag{28}$$

$$\boldsymbol{w}|_{t=0} = \boldsymbol{W}(\boldsymbol{x}, \boldsymbol{z}), \tag{29}$$

where $\mathcal{A}$ is the gradient of phase function $\boldsymbol{\theta}$, i.e. $\mathcal{A} = D_{\boldsymbol{x}}\boldsymbol{\theta}$, and $\mathcal{I}$ is the identity matrix.

Remark 1. An important feature of the above formulation, including the equations for both large-scale and high-frequency variables, is that we do not need any closure assumption; no unknown parameter needs to be determined, in contrast to other models, e.g. , the Smagorinsky model. It provides a self-consistent system which captures the interaction between large-scale and small-scale fields. The computational cost for this coupled system of equations is still quite substantial although an adaptive scheme has been developed to speed up the computation, [see 13, for a numerical example of homogeneous turbulent flows].

Remark 2. For convenience of theoretical analysis and numerical implementation, the cell problem (27) can be further simplified by a change of variables from $\boldsymbol{w}$ to $\tilde{\boldsymbol{w}}$ by letting $\tilde{\boldsymbol{w}} = \mathcal{A}\boldsymbol{w}$. Left-multiplying equation (27) by $\mathcal{A}$ gives

$$\mathcal{A}\partial_\tau \boldsymbol{w} + \mathcal{A}D_{\boldsymbol{z}}\boldsymbol{w}\mathcal{A}\boldsymbol{w} + \mathcal{A}\mathcal{A}^\mathsf{T}\nabla_{\boldsymbol{z}} q - \frac{\nu}{\epsilon}\mathcal{A}\nabla_{\boldsymbol{z}} \cdot (\mathcal{A}\mathcal{A}^\mathsf{T}\nabla_{\boldsymbol{z}}\boldsymbol{w}) = \boldsymbol{0}.$$

Since $\mathcal{A}$ does not depend on τ or $\boldsymbol{z}$,

$$\mathcal{A}\partial_\tau \boldsymbol{w} = \partial_\tau \mathcal{A}\boldsymbol{w} = \partial_\tau \tilde{\boldsymbol{w}}.$$

Further, we note:

$$\mathcal{A}D_{\boldsymbol{z}}\boldsymbol{w}\mathcal{A}\boldsymbol{w} = (D_{\boldsymbol{z}}\tilde{\boldsymbol{w}})\tilde{\boldsymbol{w}} = (\tilde{\boldsymbol{w}}\cdot\nabla_{\boldsymbol{z}})\tilde{\boldsymbol{w}},$$
$$\mathcal{A}\nabla_{\boldsymbol{z}}\cdot(\mathcal{A}\mathcal{A}^{\mathsf{T}}\nabla_{\boldsymbol{z}}\boldsymbol{w}) = \nabla_{\boldsymbol{z}}(\mathcal{A}\mathcal{A}^{T}\nabla_{\boldsymbol{z}}\mathcal{A}\boldsymbol{w}) = \nabla_{\boldsymbol{z}}\cdot(\mathcal{A}\mathcal{A}^{T}\nabla_{\boldsymbol{z}}\tilde{\boldsymbol{w}}),$$
$$(\mathcal{A}^{T}\nabla_{\boldsymbol{z}})\cdot\boldsymbol{w} = \nabla_{\boldsymbol{z}}\cdot(\mathcal{A}\boldsymbol{w}) = \nabla_{\boldsymbol{z}}\cdot\tilde{\boldsymbol{w}}.$$

Thus, we obtain the following modified cell problem for $\tilde{\boldsymbol{w}}$:

$$\partial_\tau\tilde{\boldsymbol{w}} + (\tilde{\boldsymbol{w}}\cdot\nabla_{\boldsymbol{z}})\tilde{\boldsymbol{w}} + \mathcal{A}\mathcal{A}^{\mathsf{T}}\nabla_{\boldsymbol{z}}q - \frac{\nu}{\epsilon}\nabla_{\boldsymbol{z}}\cdot(\mathcal{A}\mathcal{A}^{\mathsf{T}}\nabla_{\boldsymbol{z}}\tilde{\boldsymbol{w}}) = \boldsymbol{0}, \tag{30}$$
$$\nabla_{\boldsymbol{z}}\cdot\tilde{\boldsymbol{w}} = \boldsymbol{0}, \tag{31}$$
$$\tilde{\boldsymbol{w}}|_{t=0} = \mathcal{A}\boldsymbol{W}(\boldsymbol{x},\boldsymbol{z}). \tag{32}$$

We remark that ϵ is not small. It is related to the resolution of large-scale variables. Since we are mainly interested in large Re's, we have $\nu \ll \epsilon$, i.e. $\nu/\epsilon \ll 1$. This is very different from the traditional homogenization theory in which one studies the limit of $\epsilon \to 0$ with ν being fixed. In this case, we would have $\nu \gg \epsilon$ and $\boldsymbol{w}$ would vanish dynamically due to strong diffusion.

3. Mathematical derivation of turbulent models

Considering that the model (22)–(29) needs considerable computational CPU time and storage space, we would like to develop a simplified multiscale model. While the new model has a comparable computational complexity as the other LES models, it needs least closure assumptions.

First of all, we state the Rivlin-Ericksen Theorem, which plays an essential role in the development of the turbulence models.

Theorem 1 (Rivlin-Ericksen). *A mapping $\widehat{T} : M^3_+ \to S^3$ is isotropic and material frame invariant if and only if it is of the form*

$$\widehat{T}(F) = \bar{T}(FF^T)$$

where the mapping $\bar{T} : S^3_+ \to S^3$ is of the form:

$$\bar{T}(B) = \beta_0(i_B)I + \beta_1(i_B)B + \beta_3(i_B)B^2$$

for every $B \in S^3_+$, where $\beta_0, \beta_1, \beta_2$ are real-valued functions of the three principal invariants i_B of the matrix B.

Proof of the Rivlin-Ericksen Theorem can be found in [17].

Note that the cell problem (30) for $\tilde{\boldsymbol{w}}$ is frame invariant, i.e. the following conditions are met:

1. translational invariance
$$\boldsymbol{x} = \boldsymbol{y} + \boldsymbol{Z}$$
where $\boldsymbol{Z}$ is a constant vector,
2. Galilean invariance
$$\boldsymbol{x} = \boldsymbol{y} + \boldsymbol{v}t,$$
where $\boldsymbol{v}$ is a constant vector,
3. rotational invariance
$$\boldsymbol{x} = M\boldsymbol{y}$$
where M is a rotation matrix with
$$(M^{\mathsf{T}}M)_{i,j} = \delta_{i,j}.$$

Define $\mathcal{B} = \mathcal{A}\mathcal{A}^{\mathsf{T}}$, which is obviously symmetric. By the Rivlin-Ericksen theorem, we have the following relation in three-dimensional space:

$$\langle \tilde{\boldsymbol{w}} \otimes \tilde{\boldsymbol{w}} \rangle(\mathcal{B}) = a_0\mathcal{I} + a_1\mathcal{B} + a_2\mathcal{B}^2. \tag{33}$$

At this point, we only know that all these coefficients are real-valued functions of the three principal invariants of $\mathcal{B}$. Furthermore, $\mathcal{B}$ cannot be solved explicitly to obtain these invariants.

However, to extract the structure of the Reynolds stress, we perform a local-in-time multiscale analysis, accounting for interaction between large and small scales through dynamic re-initialization of the phase function. The large-scale components, $\boldsymbol{u}$ and $\boldsymbol{\theta}$, can generate small scales dynamically through advection and nonlinear interaction. Thus enforcing that $\boldsymbol{u}$ contains only the large-scales, dynamic iterative reparameterization of the multiscale solution enables us to capture the interactions among all small scales. More specifically, we solve the average equations (25) for the inverse phase flow $\boldsymbol{\theta}$ in a local time interval $[t, t + \Delta t]$ with $\boldsymbol{\theta}(t, \boldsymbol{x}) = \boldsymbol{x}$ as the initial condition. By using the forward Euler method, we can approximate $\boldsymbol{\theta}$ as follows:

$$\boldsymbol{\theta}(t + \Delta t, \boldsymbol{x}) = \boldsymbol{x} - \Delta t \boldsymbol{u}(t, \boldsymbol{x}).$$

It follows that the rate of deformation can be computed as $\mathcal{A} = D_{\boldsymbol{x}}\boldsymbol{\theta} = \mathcal{I} - \Delta t \nabla \boldsymbol{u} + O(\Delta t^2)$, and its inverse $\mathcal{A}^{-1} = \mathcal{I} + \Delta t \nabla \boldsymbol{u} + O(\Delta t^2)$. The above scheme is accurate up to the second order of Δt.

Therefore, $\mathcal{B}$ can be approximated as follows:

$$\mathcal{B} = \mathcal{A}\mathcal{A}^{\mathsf{T}} = \mathcal{I} - 2\Delta t\mathcal{D} + O(\Delta t^2), \tag{34}$$

where $\mathcal{D}$ is the strain rate tensor defined as

$$\mathcal{D} = \frac{1}{2}\left(\nabla \boldsymbol{u} + \nabla \boldsymbol{u}^{\mathsf{T}}\right).$$

Then we have the approximation of $\langle \tilde{\boldsymbol{w}} \otimes \tilde{\boldsymbol{w}} \rangle$

$$\begin{aligned}
\langle \tilde{\boldsymbol{w}} \otimes \tilde{\boldsymbol{w}} \rangle &= a_0\mathcal{I} + a_1\mathcal{B} + a_2\mathcal{B}^2 \\
&= a_0\mathcal{I} + a_1(\mathcal{I} - 2\Delta t\mathcal{D} + O(\Delta t^2) + a_2(\mathcal{I} - 2\Delta t\mathcal{D} + O(\Delta t^2)^2 \\
&= \alpha\mathcal{I} - \tilde{\beta}\Delta t\mathcal{D} + O(\Delta t^2),
\end{aligned}$$

where the coefficients $\alpha = a_0 + a_1 + a_2$ and $\tilde{\beta} = 2(a_1 + 2a_2)$. Note that both α and $\tilde{\beta}$ are functions of the invariants of $\mathcal{B}$.

Finally, the Reynolds stress tensor is

$$\begin{aligned}
\mathcal{R} &= \langle \boldsymbol{w} \otimes \boldsymbol{w} \rangle \\
&= \langle \mathcal{A}^{-1}\tilde{\boldsymbol{w}} \otimes \mathcal{A}^{-1}\tilde{\boldsymbol{w}} \rangle \\
&= \langle (\mathcal{I} + \Delta t\nabla \boldsymbol{u} + O(\Delta t^2))\tilde{\boldsymbol{w}} \otimes (\mathcal{I} + \Delta t\nabla \boldsymbol{u} + O(\Delta t^2))\tilde{\boldsymbol{w}} \rangle \\
&= \langle \tilde{\boldsymbol{w}} \otimes \tilde{\boldsymbol{w}} \rangle + \Delta t\nabla \boldsymbol{u}\langle \tilde{\boldsymbol{w}} \otimes \tilde{\boldsymbol{w}} \rangle + \Delta t\langle \tilde{\boldsymbol{w}} \otimes \tilde{\boldsymbol{w}} \rangle \nabla u^{\mathsf{T}} + O(\Delta t^2) \\
&= \alpha\mathcal{I} - \beta\Delta t\mathcal{D} + O(\Delta t^2).
\end{aligned} \tag{35}$$

where $\mathrm{tr}(\mathcal{R}) = \alpha/3 = (a_0 + a_1 + a_2)/3$ is the SGS kinetic energy, and $\beta = -2(a_0 - a_2)$. Both are also functions of the invariants of $\mathcal{B}$.

Remark 3. The expression for Reynolds stress (35) applies to various flows, as long as the cell problem (30) is frame invariant. This is true for both homogeneous and channel flows. However, the coefficient β depends on the flow properties, such as geometry. In Section 4, we will look into the specific expression of β.

Remark 4. Since $\nabla \cdot (\alpha\mathcal{I}) = \nabla\alpha$, the first term $\alpha\mathcal{I}$ in (35) can be integrated into the pressure term in (22) with a modified pressure $p' = p + \alpha$.

Lemma 1. *The coefficient β in* (35) *is of order* $1/\Delta t$*, i.e.*

$$\beta \sim \frac{1}{\Delta t}.$$

This lemma can be verified using the linear relation between $\mathcal{R}$ and $\mathcal{D}$ in (35) and its proof can be found in [14].

Remark 5. Note that in the limite $\Delta t \to 0$, the Reynolds stress tensor should not reduce to a multiple of identity matrix, which means that $\mathcal{R}$ must have an $O(1)$ effect on the LES model (22). By Lemma 1, β is of order $1/\Delta t$, or

$$\beta \Delta t \sim \ 1.$$

Therefore, the term $-\beta \Delta t \mathcal{D}$ does not vanish when taking the limit $\Delta t \to 0$.

In eddy-viscosity models, the stress tensor is assumed to be a linear functional of the strain rate tensor via the turbulent eddy viscosity ν_τ

$$\tilde{\mathcal{R}}_{ij} = \mathcal{R}_{ij} - \frac{1}{3} R_{kk} \delta_{ij} = -\nu_\tau \mathcal{D}_{ij}, \tag{36}$$

which is a first-order approximation, as is that in (35). We remark that such linear relation between the stress and strain rate tensor is not meant to be valid pointwise, but should be understood in a statistical sense as ensemble average. To demonstrate this, the channel flow is taken as an example. The computational settings in [18] are adopted. The streamwise (x) and spanwise (z) computational periods are chosen to be 4π and 2π, and the half-width of the channel is 1, i.e. , the computational domain is $[0, 4\pi] \times [-1, 1] \times [0, 2\pi]$. Figure 1 shows the spatial distributions of sign of $\tilde{\mathcal{R}}_{11} \mathcal{D}_{11}$ on the channel center $y = 0$. Figure 1(a) is the time average of the sign at each grid point, while figure 1(b) displays the snapshot of the sign on the central plane at $t = 2$. Hence, there does not exist a positive ν_τ such that (36) holds pointwise, [see 14, for more discussion].

Furthermore, ν_τ is assumed to be positive, which treats the 'dissipation' of kinetic energy at sub-grid scales similar to viscous (molecular) dissipation. As a matter of fact, the Reynolds stress term reflects neither diffusion nor dissipation locally in space, but reflects equivalent, ensemble averaged effects of turbulent fluctuations. Figure 2 indicates that each element of $\tilde{R}$ and its counterpart of $\mathcal{D}$ do not always have the same signs in time. The eddy-viscosity model (36) could be improved by allowing ν_τ to change sign. Germano *et al.* [19] allowed subgrid-scale eddy viscosity ν_τ to change sign dynamically based on a two-level grid and demonstrated that it indeed gives improved results by incorporating the backscattering effect. Since the two-level dynamic Smagorinsky model also introduces other errors such as interpolation error and its implementation is more involved, we will restrict our

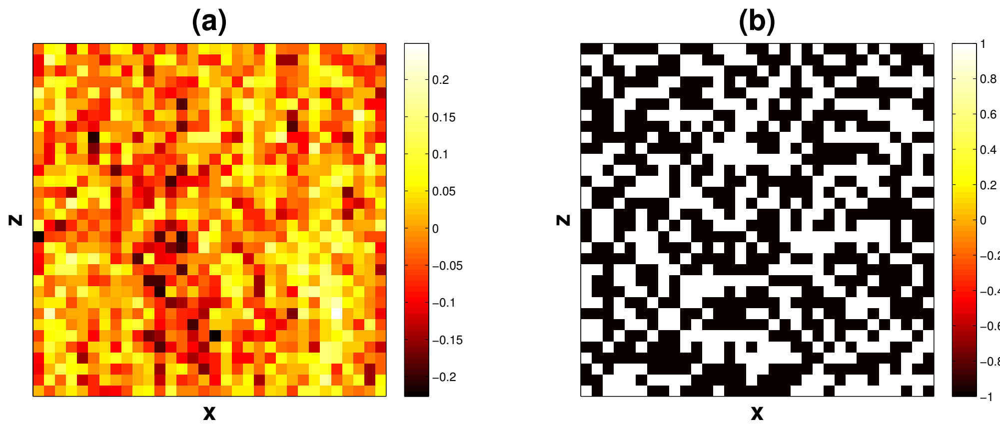

Figure 1: Spatial distributions of sign of $\tilde{\mathcal{R}}_{11}\mathcal{D}_{11}$ on the central layer of the channel $y = 0$. Left: time average over time interval [0.2, 2]; Right: a snapshot at $t = 2$.

discussions here to the Smagorinsky model by enforcing ν_τ to be positive. In Section 4, we will look for a simplified model with dissipative effect.

Remark 6. In (35), we establish a linear constitutive relation between the Reynolds stress $\tilde{\mathcal{R}}$ and the mean strain rate $\mathcal{D}$, up to second order accuracy in time step Δt. The first term $\alpha\mathcal{I}$ is not crucial since this can be incorporated as a modified pressure. Hereafter, we write $\tilde{\mathcal{R}}$ as $\mathcal{R}$ for simplicity. The remaining question is how to determine the coefficient β, for which we need to know the detailed structure of the symmetric tensor $\mathcal{B}$. Constitutive relation necessarily involves material property like viscosity.

Note that there exists a relation between $\mathcal{B}$ and $\mathcal{D}$ given in (34), so we can find the relation of the eigenvalues of $\mathcal{B}$ and $\mathcal{D}$ as follows. In three dimensions, assume λ_i and $\tilde{\lambda}_i\,(i = 1, 2, 3)$ are the eigenvalues of $\mathcal{D}$ and $\mathcal{B}$, respectively, while $\psi_i\,(i = 1, 2, 3)$ are the corresponding eigenfunctions. Then, up to the

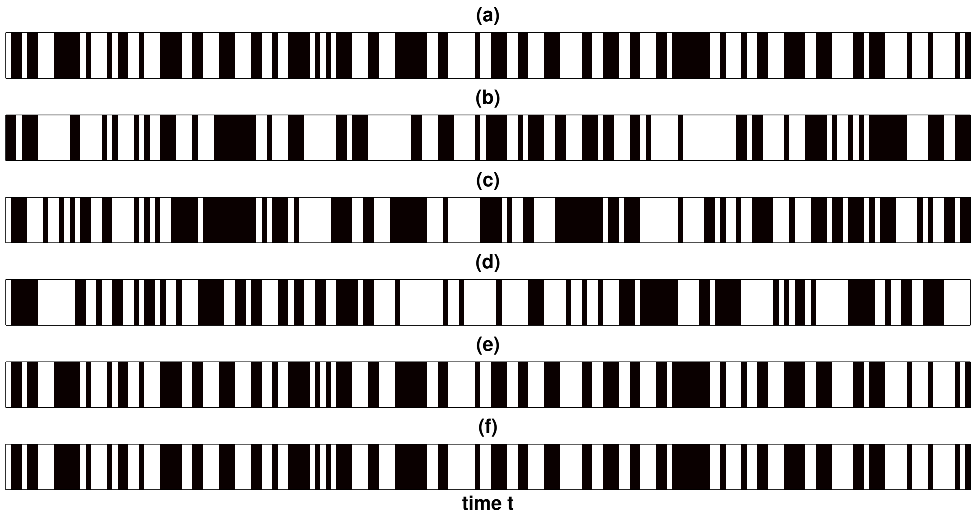

Figure 2: Time series of sign of $\tilde{\mathcal{R}}\mathcal{D}$ elements at location (3.81, 0, 1.90) over time interval $[0.2, 2]$. Black bars denote -1 and white bars denote $+1$. (a) $\tilde{\mathcal{R}}_{11}\mathcal{D}_{11}$; (b) $\tilde{\mathcal{R}}_{22}\mathcal{D}_{22}$; (c) $\tilde{\mathcal{R}}_{33}\mathcal{D}_{33}$; (d) $\tilde{\mathcal{R}}_{12}\mathcal{D}_{12}$; (e) $\tilde{\mathcal{R}}_{23}\mathcal{D}_{23}$; (f) $\tilde{\mathcal{R}}_{31}\mathcal{D}_{31}$.

second order of Δt,

$$\mathcal{B}\psi_i = (\mathcal{I} - \Delta t \mathcal{D})\psi_i = \tilde{\lambda}_i \psi_i, \quad i = 1, 2, 3,$$

which gives

$$\mathcal{D}\psi_i = \frac{1 - \tilde{\lambda}_i}{\Delta t}\psi_i = \lambda_i \psi_i, \quad i = 1, 2, 3,$$

or

$$\tilde{\lambda}_i = 1 - \Delta t \lambda_i, \quad i = 1, 2, 3. \tag{37}$$

Further, the three invariants I_i, $(i = 1, 2, 3)$ of a matrix M can be expressed by the three eigenvalues λ_i, $(i = 1, 2, 3)$ as follows

$$\begin{aligned} I_1 &= \mathrm{tr}(M) = \sum_{i=1,2,3} \lambda_i, \\ I_2 &= \frac{1}{2}\left((\mathrm{tr}(M))^2 - \mathrm{tr}(MM)\right) = \lambda_1\lambda_2 + \lambda_2\lambda_3 + \lambda_3\lambda_1, \\ I_3 &= \det(M) = \prod_{i=1,2,3} \lambda_i. \end{aligned}$$

Given the relations (37), we can express the invariants of $\mathcal{B}$ by those of $\mathcal{D}$. Now, the coefficient β can be formulated approximately as a function of the three principal invariants of $\mathcal{D}$. For various flows, we can specify the characteristic structure of the strain rate tensor $\mathcal{D}$ to obtain an explicit form of β. To validate our mathematical derivation of turbulent models, we first take homogeneous turbulent flow as an example for its simple geometry and physics. Later on, we will address the more realistic channel flow, chosen because of its relevance to a large variety of engineering applications and its ability to provide direct insight into fundamental turbulence phenomena. We will investigate these two examples further in section 4.

4. Examples: Incompressible homogeneous turbulence and turbulent channel flow

4.1. Homogeneous incompressible turbulence

For homogeneous turbulence, the statistics are spatially homogeneous and isotropic. Hence, all entries in the averaged strain tensor must be of the same order. Then, the full averaged $\mathcal{D}$ has to be considered:

$$\mathcal{D} = \begin{bmatrix} u_x & \frac{1}{2}(u_y + v_x) & \frac{1}{2}(u_z + w_x) \\ \frac{1}{2}(u_y + v_x) & v_y & \frac{1}{2}(v_z + w_y) \\ \frac{1}{2}(u_z + w_x) & \frac{1}{2}(v_z + w_y) & w_z \end{bmatrix}. \tag{38}$$

The first principal invariant of $\mathcal{D}$ is zero due to incompressibility, i.e. ,

$$I_1 = \mathrm{tr}(\mathcal{D}) = \nabla_{\boldsymbol{x}} \cdot \boldsymbol{u} = 0.$$

The other two invariants can be calculated as follows:

$$I_2 = \frac{1}{2}\left((\mathrm{tr}(\mathcal{D}))^2 - \mathrm{tr}(\mathcal{D}\mathcal{D})\right) = -\frac{1}{2}\left\|\mathcal{D}\right\|_F^2, \quad I_3 = \det(\mathcal{D}). \tag{39}$$

where $\|\cdot\|_F$ is the Frobenius norm, i.e. , $\|\mathcal{D}\|_F = \sqrt{\sum_i \sum_j |\mathcal{D}_{ij}|^2}$. It was reported in [20] that the determinant of $\mathcal{D}$, i.e. , I_3, vanishes in the statistical sense. However, for each snapshot of homogeneous turbulence, the determinant of $\mathcal{D}$ is not expected to vanish in general. Therefore, mathematically, the choice of β cannot be determined explicitly. From dimensional analysis, we find that β has the dimension of $(-2I_2)^{1/2} = \|\mathcal{D}\|_F$ or $I_3^{1/3} = (\det(\mathcal{D}))^{1/3}$. To find out the proper form of β, we assume that β is a linear function of $\|\mathcal{D}\|_F$ or $(\det(\mathcal{D}))^{1/3}$, i.e. ,

Table 1: Quantitative order of the velocity derivatives.

$\partial u/\partial x$	$\partial u/\partial y$	$\partial u/\partial z$	$\partial v/\partial x$	$\partial v/\partial y$	$\partial v/\partial z$	$\partial w/\partial x$	$\partial w/\partial y$	$\partial w/\partial z$
$\sim 10^{-2}$	$\sim 10^{2}$	$\sim 10^{-2}$	$\sim 10^{-4}$	$\sim 10^{-1}$	$\sim 10^{-4}$	$\sim 10^{-2}$	$\sim 10^{2}$	$\sim 10^{-1}$

$$\beta(I_1, I_2, I_3) = C_1^2 \left\|\mathcal{D}\right\|_F,$$

or

$$\beta(I_1, I_2, I_3) = C_2(\det(\mathcal{D}))^{1/3},$$

where C_1 and C_2 are universal constants due to homogeneity. Using the minimization technique described in Section 4.2, it is found that when choosing the norm $\left\|\mathcal{D}\right\|_F$ for β, C_1 is noticeably uniform, while C_2 shows a distinctly inhomogeneous pattern. Although we cannot justify the use of the Frobenius norm mathematically, this is definitely an indicator of preference for the Frobenius norm over the determinant from this numerical study [see 14, for more details].

Note that Lemma 1 shows that $\beta \sim 1/\Delta t$. Then based on dimensional analysis and numerical verification above, we assume that β is a linear function of $\left\|\mathcal{D}\right\|_F$, i.e. ,

$$\beta(I_1, I_2, I_3) = (C_s\Delta)^2 \left\|\mathcal{D}\right\|_F / \Delta t,$$

where C_s is a universal constant and Δ is a typical length for the large-scale solutions. Finally, we recover the Smagorinsky model for homogeneous turbulence, up to second-order accuracy of time step,

$$\mathcal{R} = -(C_s\Delta)^2 \left\|\mathcal{D}\right\|_F \mathcal{D}.$$

4.2. Channel flow

The argument for homogeneous turbulence also applies to the channel flow. This leads to the following modified Smagorinsky model:

$$\mathcal{R} = -\beta\Delta t\mathcal{D}.$$

We can simplify the Smagorinsky model by taking advantage of the structure of the strain rate $\mathcal{D}$ for channel flow. Specifically, by an asymptotic boundary layer analysis, we find:

$$\frac{\partial u}{\partial y}, \frac{\partial w}{\partial y} \gg \frac{\partial u}{\partial x}, \frac{\partial u}{\partial z}, \frac{\partial v}{\partial y}, \frac{\partial w}{\partial x}, \frac{\partial w}{\partial z} \gg \frac{\partial v}{\partial x}, \frac{\partial v}{\partial z}.$$

This scaling analysis of the velocity derivatives near the wall is consistent with results obtained by DNS (see Table 1). Given the orders of the velocity derivatives, we neglect the small quantities in the entries of $\mathcal{D}$. Thus, $\mathcal{D}$ can be approximated as

$$\mathcal{D} \sim \begin{bmatrix} 0 & u_y/2 & 0 \\ u_y/2 & 0 & w_y/2 \\ 0 & w_y/2 & 0 \end{bmatrix}. \tag{40}$$

The eigenvalues of the above approximate $\mathcal{D}$ are $\lambda_1 = 0$, $\lambda_{2,3} = \pm\frac{1}{2}\sqrt{u_y^2 + w_y^2}$. Thus it follows that the three principal invariants are $I_1 = I_3 = 0$, $I_2 = -(u_y^2 + w_y^2)/4$. Now, the coefficients α and β are functionals of I_2 or $u_y^2 + w_y^2$ only. Based on the same arguments used for the homogeneous turbulence, we propose:

$$\beta = \frac{\Delta^2}{\Delta t} f(y)(u_y^2 + w_y^2)^{1/2},$$

where $f(y)$ is a function of y or y^+ due to inhomogeneity in the normal direction. Using DNS data, Figure 3 shows that $f(y^+)$ has the shape close to the van Driest damping function

$$f(y^+) = C_m^2((1 - \exp(-y^+/A)))^2,$$

where C_m is a universal constant and $A = 25$ is the van Driest constant [2]. The distance from the wall is defined as follows

$$y^+ = \frac{u_\tau(\delta - |y|)}{\nu}, \tag{41}$$

where δ is the channel half-width, u_τ is the friction velocity, and ν is the viscosity.

Finally, based on the multiscale analysis, we propose a simplified model for the Reynolds stress

$$\mathcal{R} = -(C_m\Delta(1 - \exp(-y^+/A)))^2(u_y^2 + w_y^2)^{1/2}\mathcal{D}. \tag{42}$$

Remark 7. In the simplified model (42), the Reynolds stress reduces to 0 as the wall is approached due to van Driest damping function [2, 21, 22]. This ensures that the non-slip boundary condition on walls is preserved.

The constant C_m can be determined by locally minimizing the Reynolds stress error term

$$\min_{C_m} \left\| R + \left(C_m\Delta(1 - \exp(-y^+/A))(u_y^2 + w_y^2)^{1/4}\right)^2 \mathcal{D} \right\|_F.$$

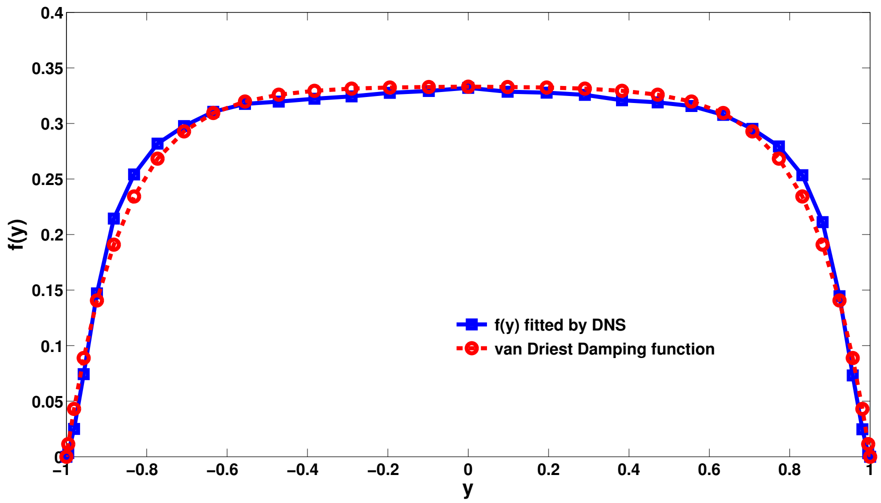

Figure 3: Profile of $f(y)$ from DNS vs. van Driest function

This gives us

$$C_m = \frac{\sqrt{-\mathcal{R} : \mathcal{D}}}{\Delta(1 - \exp(-y^+/A))(u_y^2 + w_y^2)^{1/4} \left\|\mathcal{D}\right\|_F}, \tag{43}$$

where $\mathcal{R} : \mathcal{D} = \sum_{i,j} \mathcal{R}_{ij}\mathcal{D}_{ij}$. We perform *a priori* computation to determine C_m in (43) using the multiscale formulation in the following algorithm.

Algorithm 1 (Determining the constant C_m).

i. *Run a DNS of* (1) *to get the full velocity field* $\boldsymbol{u}^\epsilon(\boldsymbol{x}_i, t_n)$ *at each time step,*

ii. *Perform a reparameterization procedure, based on the Fourier expansion and explained in detail in Appendix A for the channel flow, to obtain* $\boldsymbol{u}(\boldsymbol{x}_i, t_n)$ *and* $\boldsymbol{w}(\boldsymbol{x}_i, t_n, \boldsymbol{x}_i/\epsilon, t_n/\epsilon)$*,*

iii. *The Reynolds stress is*

$$\mathcal{R}(\boldsymbol{x}, t) = \langle \boldsymbol{w} \otimes \boldsymbol{w} \rangle - \frac{1}{3}\mathrm{tr}(\langle \boldsymbol{w} \otimes \boldsymbol{w} \rangle)\mathcal{I}. \tag{44}$$

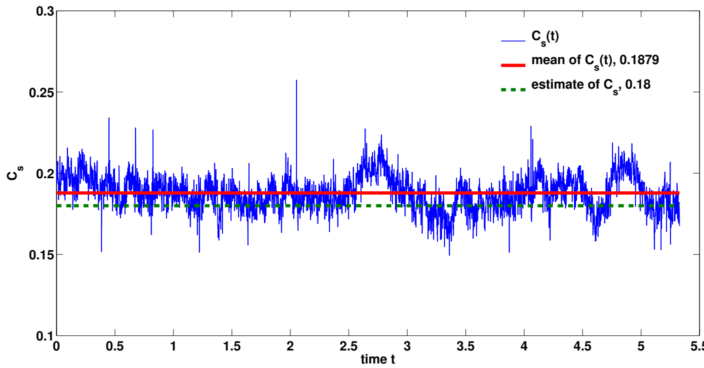

Figure 4: Temporal evolution of C_s with van Driest damping function for channel flow. The flat solid line denotes the value of 0.1879, the time average of $C_s(t)$. The dashed line denotes 0.18.

4.3. Verification of the Algorithm 1 and determination of constant C_m

To validate the algorithm 1, we run a test on a classical eddy viscosity model–the Smagorinsky model with van Driest damping:

$$\mathcal{R} = -(C_s\Delta(1-\exp(-y^+/A)))^2 \left\|\mathcal{D}\right\|_F \mathcal{D}. \tag{45}$$

For the channel flow, the layer near the wall introduces a large amount of dissipation. The extra dissipation prevents the formation of the eddies [23], thus eliminating turbulence from the beginning. Therefore, the van Driest damping is introduced to reduce the Smagorinsky constant C_s to 0 when approaching the walls. For more discussions, see[21, 6]. Usually, C_s is taken to be the same as that in homogeneous turbulence, which is 0.18.

On the other hand, using an iterative homogenization of large and small scale solutions dynamically and locally minimizing the Reynolds stress error, C_s can be determined from DNS data.

Figure 4 plots the evolution of C_s. Note that C_s oscillates slightly around the value of 0.18, showing that algorithm 1 determines C_s accurately. Figure 5 indicates that the constant C_m is around 0.2074 - the value used in the following numerical simulation.

4.4. Numerical results of channel flow

The two most prominent structural features of the near-wall turbulence are illustrated in figures 6:

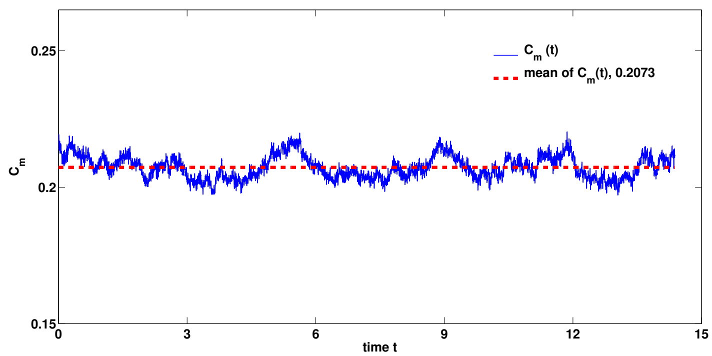

Figure 5: Temporal evolution of C_m obtained by Algorithm 1 for channel flow. The dashed line denotes 0.2073, a universal constant for the turbulent channel flow.

1. Streaks of low momentum fluid region of $u' = u(x, y, z) - U(y) < 0$, which have been lifted into the buffer region by the vortices. Here, $U(y)$ is mean velocity averaged in x and z directions:

$$U(y) = \int_{x,z} u(x, y, z) dxdz.$$

2. Elongated streamwise vortices, identified by the region of negative λ_2 proposed by Jeong and Hussain [24].

Currently, it is well accepted that near wall streamwise vortices by Biot-Savart induction lift the low speed fluid to form the streaks. On the other hand, the streamwise vortices are generated from the many normal-mode-stable streaks via a new scenario, identified by the streak transient growth (STG) mechanism [for details, see 23]. The phase averages of the vortices, their characteristics and their dynamical role have been discussed by Jeong et al. [25]. Figure 6 is quite consistent with these details of near-wall structures. These and additional features of the flow are discussed in [14].

Figure 7 shows the profile of the mean velocity normalized by the friction velocity u_τ for $Re_\tau = 180$. In the viscous sublayer $y^+ < 10$, we observe excellent agreement with the linear relation $u^+ = y^+$. In the log-region ($y^+ > 30$, $y/\delta < 0.3$), the well known logarithmic law of von Kármán [29]

$$u^+ = \frac{1}{\kappa} \ln y^+ + B,$$

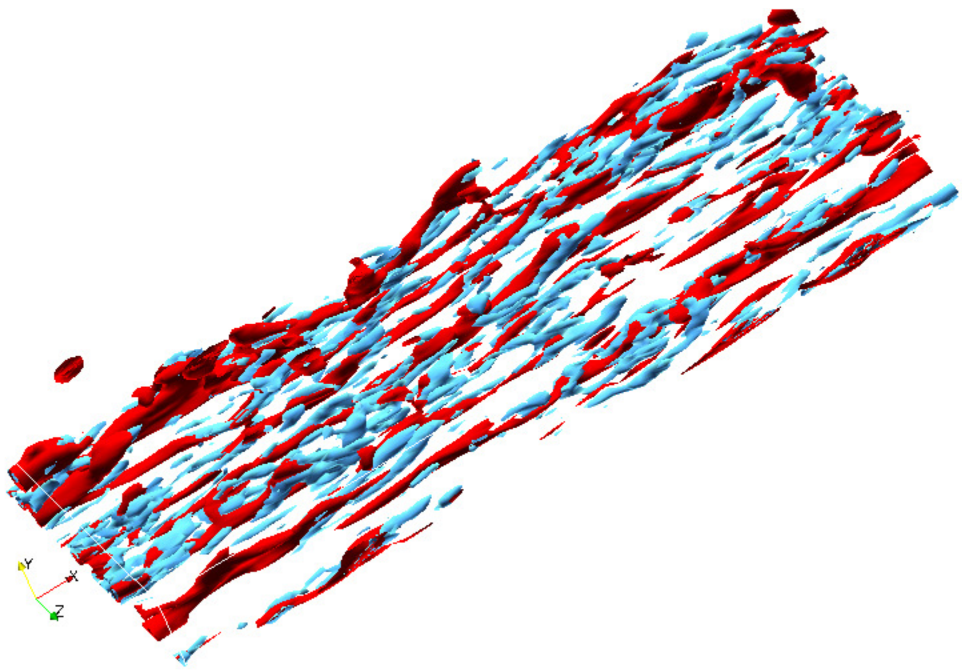

Figure 6: Turbulent structure near the wall obtained using simplified Smagorinsky model; Iso-surfaces of streamwise vortices (blue) by the λ_2 definition ($\lambda_2 = -\lambda_{\text{rms,max}} = -176.54$) [24] and lifted low-speed streaks (red) denote $u' < 0$ in the region $0 < y^+ < 60$, $Re_\tau = 180$.

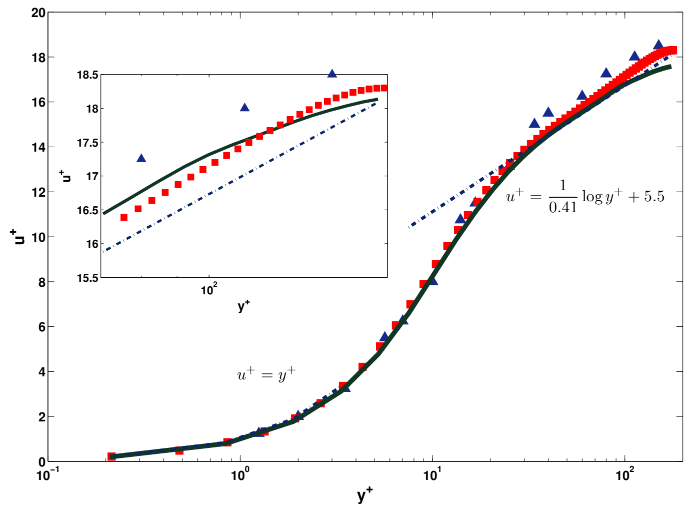

Figure 7: Mean streamwise velocity u^+ for $Re_\tau = 180$. $\triangle$, experiment by Eckelmann [26]; $\square$, DNS by Kim et al. [18]; solid line, simplified model; dash-dot line, linear relation and log-law.

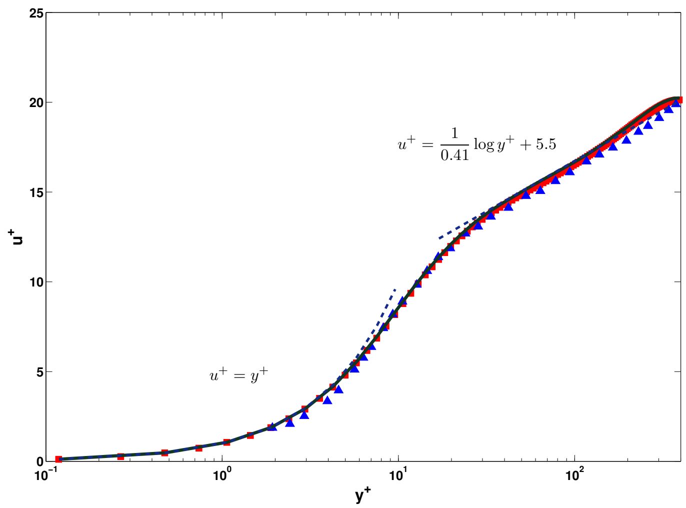

Figure 8: Mean streamwise velocity u^+ for $Re_\tau = 395$. $\Box$, DNS by Moser et al. [27]; $\triangle$, experiment by Hussain and Reynolds [28]; solid line, simplified model; dash-dot line, linear relation and log-law.

holds; where $\kappa = 0.41$ is the von Kármán constant and B is the additive constant. In the simplified Smagorinsky model, B is 5.5, the approximate value reported in the literature [26, 18, 30]. In the log-region, the profiles of mean streamwise velocity of both the simplified model and DNS by Kim et al. [18] are lower than experimental results by Eckelmann [26].

The mean velocity u^+ for $Re_\tau = 395$ is shown in figure 8 and compared to the DNS results obtained by Moser et al. [27] and the experimental results by Hussain and Reynolds [28] for $Re_\tau = 642$. In the viscous sublayer, the results of the simplified model obey the linear relation accurately. The profile conforms to the log law with the constant $B = 5.5$, while both DNS by Moser et al. [27] and our simplified model give slightly larger values of u^+ than the experiments by Hussain and Reynolds [28].

We have also performed detailed comparison of our simplified turbulent model with those obtained by DNS [18, 27] and experiments [28, 26, 31, 32, 33, 34] for flow quantities such as the mean velocity profiles, r.m.s. velocity and vorticity fluctuations, turbulent kinetic energy budget, etc. in turbulent channel flow. Our results are in good qualitative agreement with DNS and experiments. These results are reported in [14].

5. Summary and discussion

We presented a new mathematical derivation of a closure relating the Reynolds stress to the mean strain rate for incompressible turbulent flows. This derivation is based on a multiscale analysis of the Navier-Stokes equation. By using a systematic multiscale analysis and an iterative homogenization of the large and small scale solutions dynamically, we identified a crucial structure of the Reynolds stress. As a consequence, we have established a linear constitutive relationship between the Reynolds stress and the strain rate for incompressible turbulent flows to the leading order. Further consideration of specific flows produced an explicit formula for the Reynolds stress in two examples: homogeneous turbulence and channel flow. The Smagorinsky model for homogeneous turbulence has been recovered using this mathematical derivation. In addition, we have developed a simplified Smagorinsky model for channel flow.

A numerical study has been performed to validate the simplified model for channel flow. For profiles of the mean velocity, the results obtained by the simplified model are in good agreement with both experimental and DNS results at $Re_\tau = 180$ and $Re_\tau = 395$. More numerical study of the simplified model is reported in [14], which shows good qualitative agreement with DNS and experiments.

This procedure of mathematical derivation of models has been successfully applied to turbulent flow with a relatively simple geometry. It leads to improved understanding of the physical mechanisms in the flow. Moreover, the analysis is quite general and can be applied to different geometries, and for other types of flows such as compressible and non-Newtonian flows.

Acknowledgments. This research was in part supported by a NSF Grant DMS-0908546 and by an AFOSR MURI Grant FA9550-09-1-0613. We would like to thank Professor Olivier Pironneau for many stimulating and inspiring discussions. His comments and suggestions have played an essential role in this work. We also thank Dr. Daniel Chung for providing the DNS code of turbulent channel flow.

Appendix A. Reparameterization of initial velocity in a two-scale structure

We show how to reformulate any velocity $\boldsymbol{v}(x, y, z)$, which may contain infinitely many scales, in a two-scale structure. Assume $\boldsymbol{v}$ is periodic in x and z. The no-slip boundary condition is applied in y direction. Since this procedure can be done direction by direction, we can reparameterize in the periodic direction x and z as was done in [12, 13]. Thus, we only need to deal with the non-periodic direction y. The key idea is to use the Sine transform, which not only has the same computational complexity as that of the Fourier transform, but also incorporates the boundary condition naturally.

Let $\boldsymbol{v}(x, y, z)$ be any function, which is periodic in (x, z) and zero on the boundaries in y, i.e. $\boldsymbol{v}(x, 0, z) = \boldsymbol{v}(x, 1, z) = 0$. Denote $\boldsymbol{x} = (x, y, z)$ and $\boldsymbol{k} = (k_x, k_y, k_z)$. By applying the Fourier transform in the x and z directions and the sine transform in the y-direction, we can express $\boldsymbol{v}(x, y, z)$ as follows:

$$\boldsymbol{v}(x, y, z) = \sum_{\boldsymbol{k}=(k_x,k_y,k_z)} \hat{\boldsymbol{v}}_k \sin(\pi k_y y) \exp(2\pi i(k_x x + k_z z)).$$

Choose $0 < \epsilon = 1/E < 1$, where E is an integer, and let

$$\Lambda_E = \left\{ \boldsymbol{k}; |k_j| \leq \frac{E}{2}, j = (x, y, z) \right\}, \quad \Lambda'_E = Z^3 \backslash \Lambda_E. \tag{A.1}$$

By splitting the summation into two parts in the spectral space, the velocity can be rewritten as

$$\boldsymbol{v} = \boldsymbol{v}^{(l)}(\boldsymbol{x}) + \boldsymbol{v}^{(s)}(\boldsymbol{x}, \boldsymbol{x}/\epsilon), \tag{A.2}$$

where

$$\boldsymbol{z} = \boldsymbol{x}/\epsilon = (x/\epsilon, y/\epsilon, z/\epsilon)$$

The two terms in (A.2) are the large-scale velocity and the small-scale velocity respectively,

$$\boldsymbol{v}^{(l)}(\boldsymbol{x}) = \sum_{\boldsymbol{k}\in\Lambda_E} \hat{\boldsymbol{v}}(\boldsymbol{k}) \sin(\pi k_y y) \exp(2\pi i(k_x x + k_z z)),$$
$$\boldsymbol{v}^{(s)}(\boldsymbol{x}, \boldsymbol{y}) = \sum_{\boldsymbol{k}\in\Lambda'_E} \hat{\boldsymbol{v}}(\boldsymbol{k}) \sin(\pi k_y y) \exp(2\pi i(k_x x + k_z z)).$$

By rewriting each $\boldsymbol{k}$ in the following form

$$\boldsymbol{k} = E\boldsymbol{k}^{(s)} + \boldsymbol{k}^{(l)},$$

where

$$\boldsymbol{k}^{(s)} = (k_x^{(s)}, k_y^{(s)}, k_z^{(s)}), \quad \boldsymbol{k}^{(l)} = (k_x^{(l)}, k_y^{(l)}, k_z^{(l)}),$$

we have

$$\begin{aligned}
v^{(s)} &= \sum_{\boldsymbol{k}\in\Lambda'_E} \hat{\boldsymbol{v}}(\boldsymbol{k}) \sin\left(\pi k_y y\right) \exp\left(2\pi i(k_x x + k_z z)\right) \\
&= \sum_{E\boldsymbol{k}^{(s)}+\boldsymbol{k}^{(l)}\in\Lambda'_E} \hat{\boldsymbol{v}}(E\boldsymbol{k}^{(s)} + \boldsymbol{k}^{(l)}) \sin\left(\pi(Ek_y^{(s)} + k_y^{(l)})y\right) \\
&\qquad \times \exp\left(2\pi i((Ek_x^{(s)} + k_x^{(l)})x + (Ek_z^{(s)} + k_z^{(l)})z)\right) \\
&= \sum_{\boldsymbol{k}^{(s)}\neq 0} \left(\sum_{\boldsymbol{k}^{(l)}\in\Lambda_E} \hat{\boldsymbol{v}}(E\boldsymbol{k}^{(s)} + \boldsymbol{k}^{(l)}) \sin\left(\pi k_y^{(l)} y\right) \exp\left(2\pi i(k_x^{(l)} x + k_z^{(l)} z)\right) \right) \\
&\qquad \times \cos\left(\pi k_y^{(s)}(Ey)\right) \exp\left(2\pi i(k_x^{(s)} Ex + k_z^{(s)} Ez)\right) \\
&+ \sum_{\boldsymbol{k}^{(s)}\neq 0} \left(\sum_{\boldsymbol{k}^{(l)}\in\Lambda_E} \hat{\boldsymbol{v}}(E\boldsymbol{k}^{(s)} + \boldsymbol{k}^{(l)}) \cos\left(\pi k_y^{(l)} y\right) \exp\left(2\pi i(k_x^{(l)} x + k_z^{(l)} z)\right) \right) \\
&\qquad \times \sin\left(\pi k_y^{(s)}(Ey)\right) \exp\left(2\pi i(k_x^{(s)} Ex + k_z^{(s)} Ez)\right) \\
&= \sum_{\boldsymbol{k}^{(s)}\neq 0} \left(\hat{\boldsymbol{v}}_1(\boldsymbol{k}^{(s)}, \boldsymbol{x}) \cos\left(\pi k_y^{(s)}(y/\epsilon)\right) + \hat{\boldsymbol{v}}_2(\boldsymbol{k}^{(s)}, \boldsymbol{x}) \sin\left(\pi k_y^{(s)}(y/\epsilon)\right) \right) \\
&\qquad \times \exp\left(2\pi i(k_x^{(s)} x/\epsilon + k_z^{(s)} z/\epsilon)\right) \\
&= \boldsymbol{v}^{(s)}\left(\boldsymbol{x}, \frac{\boldsymbol{x}}{\epsilon}\right),
\end{aligned}$$

where $\hat{\boldsymbol{v}}_1(\boldsymbol{k}^{(s)},\boldsymbol{x})$ and $\hat{\boldsymbol{v}}_2(\boldsymbol{k}^{(s)},\boldsymbol{x})$, which are defined in the physical space, are the results of the inverse transform of the large scale,

$$\hat{\boldsymbol{v}}_1(\boldsymbol{k}^{(s)},\boldsymbol{x}) = \sum_{\boldsymbol{k}^{(l)}\in\Lambda_E} \hat{\boldsymbol{v}}(E\boldsymbol{k}^{(s)}+\boldsymbol{k}^{(l)})\sin\left(\pi k_y^{(l)} y\right),$$
$$\hat{\boldsymbol{v}}_2(\boldsymbol{k}^{(s)},\boldsymbol{x}) = \sum_{\boldsymbol{k}^{(l)}\in\Lambda_E} \hat{\boldsymbol{v}}(E\boldsymbol{k}^{(s)}+\boldsymbol{k}^{(l)})\cos\left(\pi k_y^{(l)} y\right).$$

Remark 8. Note that $v^{(s)}(\boldsymbol{x},\boldsymbol{z})$ is a periodic function in $\boldsymbol{z}$ with mean zero.

References

[1] J. Smagorinsky, General circulation experiments with the primitive equations. i. the basic experiment, Monthly Weather Review 91 (1963) 99–164.

[2] E. R. van Driest, On turbulent flow near a wall, J. Aerospace Sci 23 (1956) 1007–1011.

[3] J. H. Ferziger, Large eddy simulations of turbulent flows, AIAA Journal 15(9) (1977) 1261–1267.

[4] M. Lesieur, O. Méais, New trends in large-eddy simulations of turbulence, Ann. Rev. Fluid Mech. 28 (1996) 45–82.

[5] R. S. Rogallo, P. Moin, Numerical simulation of turbulent flows, Ann. Rev. Fluid Mech. 16 (1984) 99–137.

[6] P. Sagaut, Large eddy simulation for incompressible flows, an introduction, Springer-Verlag, 2001.

[7] D. R. Chapman, Computational aerodynamics development and outlook, AIAA Journal 17 (1979) 1293–1313.

[8] P. R. Spalart, W. H. Jou, M. Strelets, S. R. Allmaras, Comments on the feasibility of LES for wings, and on a hybrid RANS/LES approach, in: First AFOSR International Conference on DNS/LES, pp. 137–147.

[9] J. S. Baggett, On the feasibility of merging LES with RANS for the near-wall region of attached turbulent flows, annual research briefs, Center for Turbulence Research, NASA Ames/Stanford University, pp. 267-277, 1998.

[10] F. Hamba, A hybrid RANS/LES simulation of turbulent channel flows, Theoret. Comput. Fluid Dyn. 16 (2003) 387–403.

[11] K. D. Squires, J. R. Forsythe, P. R. Spalart, Detached-eddy simulation of the separated flow over a rounded-corner square, J. Fluids Eng. 127 (2005) 959–966.

[12] T. Y. Hou, D. P. Yang, H. Ran, Multiscale analysis in Lagrangian formulation for the 2-D incompressible Euler equation, Discrete and Continuous Dynamical System, Series A 13 (2005) 1153–1186.

[13] T. Y. Hou, D. P. Yang, H. Ran, Multiscale analysis and computation for the three-dimensional incompressible Navier-Stokes equations, Multiscale Model. Simul. 6 (2008) 1317–1346.

[14] X. Hu, Multiscale Modeling and Computation of 3D Incompressible Turbulent Flows, Ph.D. thesis, California Institute of Technology, 2012.

[15] D. W. McLaughlin, G. C. Papanicolaou, O. R. Pironneau, Convection of microstructure and related problems, SIAM J. Appl. Math. 45 (1985) 780–797.

[16] K. B. M. Q. Zaman, A. K. M. F. Hussain, Taylor hypothesis and large-scale coherent structures, J. Fluid Mech. 112 (1981) 379–396.

[17] P. G. Ciarlet, Mathematical elasticity, Volume I: Three-dimensional elasticity, North-Holland, Elsevier Science Publisher, 1988.

[18] J. Kim, P. Moin, R. Moser, Turbulence statisitics in fully developed channel flow at low Reynolds number, J. Fluid Mech. 177 (1987) 1317–1346.

[19] M. Germano, U. Piomelli, P. Moin, W. Cabot, A dynamic subgrid-scale eddy viscosity model, Phys. Fluids A 3 (1991) 1760–1765.

[20] R. Betchov, An inequality concerning the production of vorticity in isotropic turbulence, J. Fluid Mech. 1 (1956) 497–504.

[21] S. B. Pope, Turbulent Flows, Cambridge University Press, 2000.

[22] L. C. Berselli, T. Iliescu, W. J. Layton, Mathematics of Large Eddy Simulation of Turbulent Flows, Springer, 2006.

[23] W. Schoppa, F. Hussain, Coherent structure generation in near-wall turbulence, J. Fluid Mech. 453 (2002) 57–108.

[24] J. Jeong, F. Hussain, On the identification of a vortex, J. Fluid Mech. 285 (1995) 69–94.

[25] J. Jeong, F. Hussain, W. Schoppa, J. Kim, Coherent structures near the wall in a turbulent channel flow, J. Fluid Mech. 332 (1997) 185–214.

[26] H. Eckelmann, The structure of the viscous sublayer and the adjacent wall region in a turbulent channel flow, J. Fluid Mech. 65 (1974) 429–459.

[27] R. D. Moser, J. Kim, N. N. Mansour, Direct numerical simulation of turbulent channel flow up to $re_\tau = 590$, Phys. Fluids 11 (1999) 943–945.

[28] A. K. M. F. Hussain, W. C. Reynolds, The mechanics of an organized wave in turbulent shear flow, J. Fluid Mech. 41 (1970) 241–258.

[29] T. von Kármán, Mechanische Ahnlichkeit und turbulenz, in: Proc. Third Int. Congr. Applied Mechanics, Stockholm, pp. 85–105.

[30] P. R. Spalart, Direct simulation of a turbulent boudnary layer up to $re_\theta = 1410$, J. Fluid Mech. 187 (1988) 61–98.

[31] W. W. Willmarth, Pressure fluctuations beneath turbulent boundary layers, Annual Review of Fluid Mechanics 7 (1975) 13–36.

[32] H. Kreplin, H. Eckelmann, Behavior of the three fluctuating velocity components in the wall region of a turbulent channel flow, Phys. Fluids 22 (1979) 1233–1239.

[33] E. G. Kastrinakis, H. Eckelmann, Measurement of streamwise vorticity fluctuations in a turbulent channel flows, J. Fluid Mech. 137 (1983) 165–186.

[34] J.-L. Balint, J. M. Wallace, P. Vukoslavcevic, The velocity and vorticity vector fields of a turbulent boundary layer. Part 2. Statistical Properties, J. Fluid Mech. 228 (1991) 53.